1

2

3

4

5

6

7

8

9

10

11

Improvements to the OMI near UV aerosol algorithm using A-train CALIOP and

AIRS observations

O. Torres, C. Ahn and Z. Chen

O. Torres, C. Ahn and Z. Chen

(Submitted to AMT, May 1013)

Abstract.

The height of desert dust and carbonaceous aerosols layers and, to a lesser extent, the difficulty in determining the predominant size mode of these absorbing aerosol types, are sources of uncertainty in the retrieval of aerosol properties from near UV satellite observations. The availability of independent, near-simultaneous measurements of aerosol layer height, and aerosol-type related parameters derived from observations by other A-train sensors, makes possible the use of this information as input to the OMI (Ozone Monitoring Instrument) near UV aerosol retrieval algorithm (OMAERUV). A monthly climatology of aerosol layer height derived from observations by the CALIOP (Cloud-Aerosol Lidar with Orthogonal Polarization) sensor, and real-time AIRS (Atmospheric Infrared Sounder) CO observations are used in an upgraded version of the OMAERUV algorithm. AIRS CO measurements are used as a reliable tracer of carbonaceous aerosols, which allows the identification of smoke layers in regions and seasons when the dust-smoke differentiation is difficult in the near-UV. The use of CO measurements also enables the identification of elevated levels of boundary layer pollution undetectable by near UV observations alone. In this paper we discuss the combined use of OMI, CALIOP and AIRS observations for the characterization of aerosol properties, and show an improvement in OMI aerosol retrieval capabilities.

1. Introduction

Since the discovery of the near-UV capability of absorbing aerosols detection from space over a decade ago [*Hsu et al.,* 1996*; Herman et al.,* 1997*; Torres et al.,* 1998], the UV Aerosol Index (AI), calculated from observations by the Total Ozone Mapping Spectrometer (TOMS) family of sensors, and more recently by the Ozone Monitoring

54 Instrument (OMI), has been used to map the daily global distribution of UV-absorbing

55 aerosols such as desert dust particles as well as carbonaceous aerosols generated by

56 anthropogenic biomass burning and wild fires [*Herman et al*., 1997], and volcanic ash

57 injected in the atmosphere by volcanic eruptions [*Seftor et al.,* 1999]. The AI concept

58 for aerosol detection has also been applied to other near-UV capable sensors such as

59 GOME [*Gleason et al.,* 1998; *De Graaf et al.,* 2005a], and SCIAMACHY [*de Vries et*

60 *al*., 2009; *De Graaf et al.*, 2005b].

61 In addition to the qualitative AI product, near-UV retrieval algorithms of aerosol

62 extinction optical depth (AOD) and single scattering albedo (SSA) making use satellite

63 measurement in the 330-388 nm range have been applied to the TOMS [*Torres et al*.,

64 1998, 2002] and OMI [*Torres et al.*, 2007, *Ahn et al*, 2008] observations. The quantitative

65 interpretation of the near-UV measurements in terms of aerosol absorption, however, is

66 affected by the dependency of the measured radiances on the height of the absorbing

67 aerosol layer [*Torres et al.,* 1998; *De Graaf et al., 2005a*], and the difficulty in

68 differentiating between carbonaceous and desert dust aerosol types especially over land.

69 In the absence of direct observations to diagnose the location of the aerosol layer

70 in the atmosphere the TOMS aerosol algorithm [*Torres et al,* 2002] used a transport

71 model generated climatology of aerosol layer height [*Ginoux et al*, 2001]. To

72 differentiate between absorbing aerosol types, the TOMS algorithm used geographical

73 location and surface type considerations to prescribe the most likely absorbing aerosol

74 type (carbonaceous or desert dust) present in the atmospheric column.

75 The near-simultaneity of satellite observations by a plurality of A-train sensors,

76 provides the unprecedented opportunity of combining time and space collocated radiance

observations and/or derived atmospheric parameters for global climate analysis

[*Anderson et al,* 2005]. Combined A-train measurements can also be used in inversion

algorithms to further constrain retrieval conditions, and thus reduce the need of

assumptions. CALIOP (Cloud-Aerosol Lidar with Orthogonal Polarization)

measurements of the vertical distribution of the atmospheric aerosol load, and

Atmospheric Infrared Sounder (AIRS) carbon monoxide (a reliable tracer of

carbonaceous aerosols) observations, provide information that can be used to prescribe

aerosol layer height and determine aerosol type in the OMI near UV aerosol algorithm

(OMAERUV).

In this paper we discuss the use of observations by A-train sensors CALIOP and

AIRS, on aerosol layer height and CO to provide reliable information on aerosol layer

height and aerosol type as input to OMAERUV . In section 2, we briefly describe an

improved version of the OMAERUV algorithm that utilizes CALIOP and AIRS

observations as ancillary information . A detailed description of the way AIRS CO data

is used in the OMI aerosol inversion procedure is presented in section 3, followed by a

discussion of the development of a CALIOP-based aerosol layer height climatology in

section 4, and an evaluation of the improved accuracy of OMI retrievals using

AERONET observations in section 5. Summary and final remarks are presented in

section 6.

2. The OMAERUV Algorithm

OMI is a spectrograph that measures upwelling radiances at the top of the

atmosphere in the range 270-500 nm [*Levelt et al*., 2006] since its deployment in 2004.

100   With a 2600 km across track swath and sixty viewing positions, it provided nearly daily

101   global coverage at a 13x24 km nadir resolution (28x150 at extreme off-nadir) during the

102   first three years of operation. Since mid-2007, an external obstruction to the sensor's

103   field of view, perturbing OMI measurements of both solar flux and Earth shine radiance

104   at all wavelengths, began to progressively develop. Currently, about half the sensor's

105   sixty viewing positions are affected by what is referred to as 'row anomaly', since the

106   viewing positions are associated with the row numbers on the CCD detectors. The site

107   *http://www.knmi.nl/omi/research/product/rowanomaly-background.php* provides details

108   on the onset and progression of the row anomaly.

109   The OMAERUV algorithm uses as input measured reflectances at 354 and 388

110   nm to retrieve column atmosphere values of aerosol optical depth (AOD) and single

111   scattering albedo (SSA). Ancillary information on near UV (354 and 388 nm) surface

112   albedo (A_λ), surface type, and aerosol layer height (ALH) is required. Real time AIRS

113   CO measurements are used to identify carbonaceous particles, and ALH is inferred

114   based on CALIOP measurements. The way AIRS CO and CALIOP aerosol height

115   information are used in the OMAERUV algorithm is the central theme of this paper, and

116   it is discussed at length in sections 3 and 4.

117   *-Aerosol models and forward calculations*

118   The algorithm assumes that the atmospheric aerosol column can be represented

119   by one of three aerosol types: desert dust (*DD*), carbonaceous particles (*CB*), and sulfate-

120   based (*SF*) aerosols. Each aerosol type is characterized by a fixed bi-modal spherical

121   particle size distribution [*Torres et al.,* 2007] with parameters derived from long-term

122   AERONET statistics [*Dubovik et al.,* 2002]. The relative spectral dependence of the

123 imaginary component of refractive in the 354-388 nm range, $\varDelta k$, is assumed for each

124 aerosol type [*Torres et al.,* 2007], and recently modified for the CB type to account for

125 the absorption effects of organic carbon [*Jethva and Torres,* 2011] . Each aerosol type is

126 further divided into seven sub-types to account for the variability of the imaginary

127 component of the refractive index at 388nm , k_{388}, which, in combination with the

128 assumed size distribution, translates into SSA variability.

129   Forward radiative transfer calculations of upwelling reflectance at the top of the

130 atmosphere (354 and 388 nm) for the resulting 21 aerosol models were used to generate

131 a set of look-up tables (LUT's) with nodal points in viewing geometry, aerosol optical

132 depth (AOD), aerosol single scattering albedo (SSA), and aerosol layer height (ALH).

133 *-Inversion Procedure*

134   The measured reflectances are first used to calculate the scene 388 nm Lambert

135 Equivalent Reflectivity (R_{388}) , and the absorbing Aerosol Index (*AI*) as described in

136 *Torres et al.* [2007]. To exclude sub-pixel cloud contamination effects, threshold values

137 of the difference R_{388}-A_{388}, ($\varDelta R$), are used as upper limits in the allowed aerosol-related

138 reflectivity increases beyond the value of the surface reflectance A_{388}.

139   Figure 1 shows a schematic overview of OMAERUV's retrieval procedure. At

140 each OMI pixel, the *AI*, *COI* (i.e., normalized CO column amount), and surface type

141 (source: http://www-surf.larc.nasa.gov/surf/pages/data-page.html) are used to select an

142 aerosol type. For simplicity, we define the dimensionless parameter *COI* (*CO* index) as

143 the column *CO* amount (in molecules-cm^{-2}) divided by 10^{18} molecules-cm^{-2}.

144   The absorbing aerosol type identification is achieved by examining the values of

145 *AI* and *COI* in relation to threshold values AI_0 and COI_0, that represent respectively *AI*

146 noise and background *COI* values not necessarily associated with the free troposphere

147 *CO* burden which is expected to co-exist with the lofted carbonaceous aerosols. The

148 adopted values of COI_0 are 2.2 and 1.8 for the northern and southern hemisphere

149 respectively. The value of AI_0 is 0.8 for both land and ocean conditions. As shown

150 schematically in the upper-left panel of Figure 1, the presence of carbonaceous aerosols is

151 assumed if $AI \geq AI_0$ and $COI \geq COI_0$, or for $COI > 2.8$ (2.5 in the southern hemisphere)

152 regardless of *AI* considerations. On the other hand, when $AI \geq AI_0$ and $COI < COI_0$ desert

153 dust aerosols are assumed present . If neither set of conditions are met the presence of

154 sulfate aerosols is assumed.

155   Screening of sub-pixel cloud contamination is carried out making use of *AI*, *ΔR*

156 , and the selected aerosol type in an algorithm flagging scheme that assigns confidence

157 levels on the occurrence of cloud-free conditions as shown on the upper right box of

158 Figure 1. This is done by means of an algorithm Quality Flag (QF) whose value is 0 for

159 minimum cloud presence, and has a value of 1 when it is suspected that the retrieval

160 product is affected by cloud contamination.

161   Different retrieval approaches are applied over the oceans and the continents.

162 Over the oceans, the retrieval is only carried out when either DD or CB aerosols are

163 present as indicated by the *AI* parameter. No retrieval takes place over the oceans for *AI*

164 values less than 0.8. Retrievals over land, on the other hand, are carried out under all

165 conditions regardless of the value of AI. The actual retrieval method depends on the

166 nature of the aerosol signal as indicated by the magnitude of the *AI* and *COI* parameters.

167 A two-channel method that allows the simultaneous retrieval of AOD and SSA, or, a

168 single-channel retrieval of AOD is applied depending on aerosol type and AI

169   considerations as shown on the lower right box of Figure 1. When the single-channel

170   approach is applied, a SSA of 1.0 is assumed. Retrievals results are obtained for the

171   five ALH nodal point in in the LUT's (surface, 1.5, 3, 6, and 10 km).

172   A best-guess aerosol layer height must be prescribed as the accuracy of the

173   satellite retrieved properties of absorbing aerosol types in the near UV, is highly

174   sensitive to the aerosol layer altitude   above the ground [*Torres et al.,* 1998]. The lower

175   left diagram of Figure 1 describes the steps for ALH determination. For the SF aerosol

176   type, a vertically decaying distribution is used, in which aerosol concentration is largest

177   at the surface and decreases exponentially with height. If either the DD or CB aerosol

178   type has been selected, the   best guess ALH is given by a CALIOP-based

179   climatological value (Z_{clp}) developed for this purpose, and discussed in detail in section 4.

180   If the CALIOP climatology does not provide an ALH entry, an ALH assumption is made

181   that depends on aerosol type and location as shown in Fig 1. Carbonaceous aerosols

182   layers within 30˚ of the Equator are assumed to have maximum concentration at 3 km

183   above the surface whereas mid and high-latitude (pole wards of ±45˚) smoke layers are

184   assumed to peak at 6 km. The height of smoke layers between 30˚ and 45˚ latitude in both

185   hemispheres is interpolated with latitude between 3 and 6 km. The location of desert dust

186   aerosol layers varies between 1.5 and 10 km, and is given by a multiyear climatological

187   average of Chemical Model Transport (CTM) calculations using the GOCART model

188   [*Ginoux et al,* 2001] gridded at a resolution of 2.5˚. Thus, in addition to retrievals at five

189   standard ALH values, a retrieval at the best-guess value of ALH is also reported.

190

191   **3. Combined use of OMI-AI and AIRS-CO for aerosol type identification**

192   In the near-UV, the separation between absorbing and non-absorbing aerosol

193   types is straightforward given the large sensitivity to aerosol absorption in this spectral

194   region. Differentiating between carbonaceous (fine particles) and dust (coarse particles)

195   aerosols in ocean satellite retrieval algorithms that use visible and near IR observations is

196   generally done in terms the well known Angstrom's wavelength exponent (AE)

197   [*Angstrom*, 1929], whose magnitude is inversely related to the predominant particle size.

198   Typical AE values vary from nearly zero for high concentrations of desert dust aerosols

199   to values of 2.0 or greater associated with large AOD fine size carbonaceous aerosols

200   [*Eck et al.,* 1999; *Toledano et al.,* 2011]. Satellite derived AE for aerosol type

201   differentiation over land is unreliable due to uncertainties associated with surface

202   reflectance characterization [*Levy et al.,* 2010]. Because of the short separation of the two

203   channels in the OMAERUV algorithm, the AE concept is not applicable and, therefore,

204   distinguishing between fine and coarse size mode absorbing aerosol types (i.e.,

205   carbonaceous versus desert dust aerosols) requires additional external information.

206   Although OMI reflectance measurements up to 500 nm are available their use in AE

207   calculation require a precise characterization of visible surface albedo currently

208   unavailable.

209   *3.1 Carbonaceous Aerosols Tracers*

210   Nitrogen dioxide (NO_2) and formaldehyde ($HCHO$) are important biomass

211   burning byproducts measured by OMI that could be used as carbonaceous aerosol

212   tracers. Because of their relative short lifetimes (only up to a few hours) , however, these

213   trace gas are not adequate for tracing the long-range aerosol transport . Carbon monoxide

214   (CO), on the other hand, is the second most abundant trace gas produced by biomass

215 burning [*Sinha et al.,* 2003], and has a multiday-long lifetime that makes it a suitable

216 tracer of long-range transport carbonaceous aerosols. *Luo et al.* [2010], found a clear

217 spatial correlation between Tropospheric Emission Spectrometer (TES) *CO*

218 measurements and the OMI Aerosol Index signal of the smoke plume generated by the

219 2006 Australian fires [*Torres et al.,* 2007, *Dirksen et al.,* 2009]. Satellite global daily *CO*

220 measurements are routinely produced by the Measurements of Pollution in the

221 Troposphere (MOPITT) sensor on the Terra satellite [*Pan et al.,* 1998] and by the

222 Atmospheric Infrared Sounder (AIRS) on the Aqua platform [*Aumann et al.,* 2003].

223 Because of the near-simultaneity of AIRS and OMI observations, the AIRS *CO* product

224 is used in this analysis.

225 *3.2 The AIRS CO product*

226   The AIRS sensor was deployed on May 4, 2002. It is a cross-track scanning

227 grating spectrometer that measures IR radiation at 2378 channels between 3.7 and 16 μm

228 with a 13.5 km nadir field of view [*Aumann et al.,* 2003]. AIRS' *CO* inversion uses

229 radiances in the 4.50-4.58 μm region. It is considered a robust retrieval because of its

230 strong spectral signature and weak water vapor interference with an estimated accuracy

231 of about 15% [*McMillan et al.,* 2005]. The use of cloud-clearing [*Chahine et al*, 1974]

232 allows the retrievals of global *CO* for conditions up to 80% cloudy [*Susskind et al,* 2003].

233 In this analysis we used the global daily gridded AIRS column *CO* product expressed as

234 molecules-cm^{-2} at a 1˚x1˚ resolution, available at http://daac.gsfc.nasa.gov/AIRS .

235 *3.3 Combined use of CO and AI observations*

236   The spatial distributions of tropospheric *CO* amounts and atmospheric load of

237 carbonaceous aerosols are naturally correlated as both species are generated by biomass

238 burning. On the other hand, no correlation is expected to exist between tropospheric *CO*

239 and the atmospheric aerosol burden associated with desert dust particles. An example of

240 the expected relationship between *CO* and dust and smoke aerosols in shown in Figure 2.

241 The top panel shows the global spatial distribution of the OMI *AI* on July 7, 2006. The

242 *AI* map shows pools of large *AI* values over Southeastern Canada and Eastern US

243 possibly associated with an advancing smoke layer generated by boreal fires in Canada.

244 Another large absorbing aerosol plume lingers over Equatorial Africa between the

245 Equator and about 10°S, most likely the result of agriculture-related burning practices.

246 Large AI values are also present over the arid areas of Northern Africa, the Arabian

247 Peninsula, and Central Asia, as well as over the Atlantic Ocean indicating the presence

248 of a drifting synoptic scale desert dust plume. The center panel in Fig. 2 shows the

249 AIRS-*CO* column amount as derived from AIRS observations on the same day. Note

250 that very large values of *CO* column amounts are observed over the areas dominated by

251 the presence of smoke but not over the large regions occupied by the desert dust layers.

252 The combined use of the *AI* and *COI* (as defined in section 2) parameters allows the

253 separation of smoke/dust plumes as shown on the bottom panel of Fig. 2.

254   Although this straightforward way of separating absorbing aerosol types works

255 very well in most cases, it may break down under certain circumstances. A notable case

256 when the approach fails, takes place when dust aerosols are present over a region

257 characterized by high *CO* levels associated with pollution episodes other than smoke. In

258 this case the above described approach will identify the absorbing aerosol type as smoke.

259 This situation is likely to happen over Eastern China during the spring season when the

260   normally high *CO* levels co-exist with the westerly flow of large amounts of desert dust

261   aerosols from the Gobi and Taklimakan deserts.

262   The *CO*-based aerosol type separation technique is particularly useful to pick up

263   the presence of drifting layers of carbonaceous aerosols over arid areas. One such event

264   took place on 27 August 2007 when the smoke plume of the fires in Greece moved south

265   across the Mediterranean reaching Northern Libya and Algeria [*Turquety et al.,* 2009].

266   The aerosol type map in Fig 3., obtained by the previously described method, shows the

267   unmistakable presence of the Greek fires smoke plume over Northern Africa.

268   *3.4 Boundary Layer Pollution Aerosols*

269   *CO* measurements are also used in the OMAERUV algorithm to indentify cases

270   of high amounts of carbonaceous aerosols in the boundary layer that would otherwise go

271   undetected by the *AI*. Large summer AOD values are reported by AERONET

272   observations in rapidly developing industrial regions of the world such as northeastern

273   China and northern India. Because of their low elevation these aerosols yield AI values

274   below the reliability limit (~0.8) in the near UV. In addition, because of their

275   extraordinarily large concentrations they were often mistaken as cloud contamination in

276   earlier versions of the algorithm. Correlative analysis of ground-based AOD

277   measurements and satellite *CO* measurements (not shown) indicate high correlation

278   between the two parameters. Based on this analysis OMAERUV retrievals are now

279   carried out when the measured *CO* values are larger than 2.8E18 (NH) or 2.5E18 (SH)

280   regardless of the *AI* value.

281

282   **4.   Combined use of OMI and CALIOP observations**

283   CALIOP is a three-channel lidar on board the CALIPSO platform launched in

284   April 28, 2006 in an ascending polar orbit with a 1:32 pm Equator crossing time. It

285   measures polarization insensitive attenuated backscatter at 532 and 1064 nm during both

286   day and night time. In addition, CALIOP measures polarization sensitive backscatter at

287   532 nm. CALIOP probes the atmosphere between the surface and 40 km above sea level

288   at a vertical resolution that varies between 30 and 60 m. The horizontal resolution along

289   the orbital track is 335 m [*Winker et al*., 2009]. CALIOP data is available since mid-June

290   2006 and, except for minor interruptions, continues to be available to present. In addition

291   to the attenuated backscatter profile data, CALIOP's aerosol products includes a Vertical

292   Feature Mask that characterizes particle layers as either cloud or any of several aerosol

293   types, and an aerosol optical depth product. In this study we use daytime observations of

294   the 1064 nm attenuated backscatter. Unlike AIRS global daily coverage, CALIOP's

295   narrow 335 m footprint does not allow the direct use of daily observations as no global

296   coverage is available. Therefore, developing a climatological data set is the best way to

297   make use of CALIOP provided aerosol layer height data.

298   *4.1 Collocation*

299   The OMI sensor makes observations at sixty positions (or viewing angles) across

300   the orbital track. Positions 30 and 31 are closest to nadir. At launch, CALIPSO's sub-

301   satellite point coincided with OMI's scan position 45 on the right side of the OMI scan

302   for most of the orbit at low and mid-latitudes, and the time difference between OMI and

303   CALIOP daytime observations was about 13 minutes. As the Aura satellite orbit was

304   changed to reduce the overpass time difference with that of Aqua, the OMI scan position

305   of coincidence with CALIOP's observations changed to 37 over several months, and by

306   the end of the orbital maneuver the time observation difference between CALIOP and

307   OMI decreased to about 7 minutes.

308   At the 335 m CALIOP's horizontal resolution, there are 39 CALIOP profiles of

309   attenuated backscatter per OMI-CALIOP collocation pixel (OCCP) along CALIPSO's

310   orbital track. In this work we use a specially created set of orbital files that contain

311   merged OMI and CALIOP data collocated along CALIPSO's orbital track. The OMI

312   level 2 data subset coincident with CALIOP's measurements was produced by the A-

313   Train Data Depot (ATDD) project at the Goddard Earth Sciences Data and Information

314   Services Center to address the differences in spatial, vertical, and horizontal, as well as

315   temporal scales of coverage of different instruments participating in the A-Train

316   [*Savtchenko et al.,* 2008]. The ATDD data set was augmented with CALIOP's

317   observations of attenuated backscatter at 532 and 1064 nm. In addition to the CALIOP

318   backscatter data and ancillary information, the merged orbital files contain OMI

319   measured radiances, viewing geometry, ancillary data and original retrieval results at the

320   OCCP plus four additional OMI pixels on each side of the OCCP for a total of 9 pixels.

321

322   *4.2 Cloud Screening*

323   The available CALIOP backscatter profiles per OCCP were combined to create an

324   average profile representative of the vertical distribution of the atmospheric load of

325   carbonaceous and/or desert dust aerosols over the OCCP. An attempt to minimize the

326   effect of cloud contamination on both observations was carried out by applying cloud

327   screening procedures to both OMI and CALIOP observations as described by *Chen et al*

328   [2012]. Heavily cloud contaminated OMI data was excluded by rejecting observations

329 where the OCCP derived Lambert Equivalent Reflectivity (LER) was larger than 25%.

330 The calculated average CALIOP profiles were screened for the presence of clouds by

331 excluding those layers where the resulting average backscatter was larger than 0.005. The

332 effect of noise was also excluded by rejecting layers where average backscatter was

333 smaller than 0.0015. Figure 4 shows CALIOP's average attenuated backscatter profiles

334 associated with a carbonaceous aerosol layer in South America (left panel), and a desert

335 dust layer in Northern Africa (right panel) calculated using both 532 and 1064 nm

336 CALIOP observations . While no apparent difference in sensitivity between the 532 and

337 1064 channels is observed for desert dust particles (right panel), it appears that in the

338 presence of biomass burning aerosols (left panel) the 532 nm measurement losses

339 sensitivity to aerosols near the surface If low level aerosols are not accounted for, the

340 derived aerosol layer altitude would be biased high. For that reason, in this analysis we

341 use CALIOP's 1064 nm measurements that are sensitive to the presence of carbonaceous

342 and desert dust aerosols all the way to the surface.

343

344 *4.3 Aerosol layer height calculation*

345   In reducing the CALIOP measured profiles, it was assumed that the vertical

346 structure of the tropospheric aerosol load can be represented as a single layer of

347 height*ALH*. This assumption seeks to facilitate the use of the resulting climatology as

348 input to global retrieval algorithms. Although, multiple aerosol layers are common,

349 elevated dust or carbonaceous particles are most frequently observed as single layers.

350 The parameter Z_{aer} was calculated as the attenuated-backscatter-weighted height

351 according to the expression

352
$$Z_{aer} = \sum_{i-1}^{n} H(i) \left[\frac{B_{sc}(i)}{\sum_{i=1`}^{n} B_{sc}(i)} \right] \quad (1),$$

353 where $B_{sc}(i)$, is the attenuated backscatter at height $H(i)$, and n is the number of layers

354 between the surface and 10 km. The resulting aerosol layer height was assumed to be

355 representative of the aerosol layer altitude at the OCCP. The information on aerosol layer

356 height at the fine CALIOP resolution was propagated a few hundred meters beyond the

357 OCCP. The aerosol layer height at the OCCP was also assumed to be representative of

358 the aerosol altitude at any pixel in the nine-OMI-pixel subset (i.e., within approximately

359 100 km of the OCCP in the same swath) if the presence of dust or smoke was detected

360 according to the *AI*. By the same token, if for an OCCP pixel the CALIOP height was

361 undetermined (due to excessive cloud contamination) but the *AI* on other non-OCCP

362 pixels in the same swath indicated aerosol presence the height for the corresponding

363 pixel-position from the previous across- track-scan was assumed if available. It should

364 be emphasized that the resulting aerosol height data set is not a general representation of

365 the altitude of all aerosol types but it is specifically designed to account for the height of

366 elevated carbonaceous and desert dust aerosol layers when present.

367   Figure 5 shows three examples of the resulting aerosol layer height derived from

368 1064 nm CALIOP measurements as previously described. The solid line indicates the

369 effective aerosol layer height calculated using equation (1), and the dashed line

370 represents the aerosol layer height assumed in the previous version of OMAERUV

371 algorithm [*Torres et al.,* 2007]. CALIOP's observed vertical structure of the aerosol load

372 on April 4, 2007 near the Bodele depression in the Central Saharan desert shows the

373 unmistakable signature of a rising column of dust between the surface and about 3 km at

16˚N, 12˚E is shown on the top panel of Figure 5. The airborne dust plume spreads north

and south of the source in an atmospheric layer between 3 and 5 km. The aerosol layer

height assumed in the OMAERUV algorithm is underestimated by as much as 2 km in

relation to that inferred from CALIOP observations.

The center panel illustrates the vertical structure of a smoke layer as seen by the

CALIPSO lidar on August 12, 2006 over Angola and Namibia, and the Southern Atlantic

Ocean. CALIOP observations show the westward flow of smoke from fires in Angola

and Namibia over the Southern Atlantic Ocean. The CALIOP curtain image shows a

south-north transect of the smoke layer along the western coast of Central Africa from

Angola, covering Angola's coastal waters (~12°S, 13°E), and reaching land again over

the republic of Congo's coastal area (~5°S, 11.5E). Over the central and northern sections

of the transect, the aerosol layer is clearly located above low clouds. . The smoke layer

over land generated from fires in Angola and Namibia occupies a 2.5 km thick layer that

goes from the surface (about 1 km above sea level) to 3.5 km as indicated by the

attenuated backscatter signal. The assumed aerosol layer height is consistently higher

than the CALIOP derived value.

A layer of carbonaceous aerosols as seen by the OMI and CALIOP sensors over

Central Brazil on September 30, 2007 is depicted on the bottom panel of Fig 5. The

CALIOP curtain plot depicts the vertical structure of the layer over a region between

10˚S and 30˚S along CALIOPS's orbital track. On the northern most end of the plume,

the aerosol load is located in a 1 km thick layer between 3 and 4 km above the ground,

and widens towards the south. In general, the assumed height is about 1 km higher than

the CALIOP-based estimate.

397

4.4 CALIOP-based aerosol height climatology

The procedure described in the previous section to derive an effective aerosol layer height was applied to the global   CALIOP record over the two year period from July 2006 to December 2008. The extension beyond 2008 was hindered by the loss of the OCCP resulting from the onset of the OMI row anomaly discussed in section 2. Gridded 1˚x1˚ resolution monthly averages of *ALH* were calculated. A minimum of five data points per-grid were required to produce a monthly value. Extracts from a degraded 5˚x5˚ gridded product was used to fill gaps in the original 1˚x1˚ product resulting from CALIOP's lack of global coverage and the interference of clouds. Additionally, image processing techniques using convolution and Gaussian smoothing [*Gonzalez and Woods, 1992*] were applied to reduce the noise and minimize the effect of isolated maxima and minima.

Figure 6 shows global maps of the monthly averaged aerosol layer height (Z_{clp}), in km above surface, derived from CALIOP observations. Maps shown correspond to the mid-season months (January, April, July, October).

The Z_{clp} spatial distribution in January is dominated by the presence of desert dust and carbonaceous aerosols copiously produced by their emission sources in the Saharan (desert dust) and Equatorial Africa (biomass burning). Z_{clp}'s between 3 and 4 km predominate over the northern African deserts, while values between 2 and 3 km are observed associated with the fire activity in the tropical belt along the Atlantic coast from Guinea to Nigeria, and extending eastwards to Ethiopia. Over the northern Atlantic Ocean, Z_{clp} descends rapidly westwards from over 2 km at the Northern African West

18

420   coast to the 45°W meridian, and continues to decrease, with some oscillations, to

421   minimum values of about 1 km over the Gulf of Mexico. Z_{clp}'s around 3 km can be

422   observed over the SE United States as a consequence of local fires, as well as long range

423   transport from Central America. High Z_{clp} values are also observed in the Southern

424   Hemisphere Summer over the land masses of South America (Patagonia), Western

425   Africa, and Australia where desert dust production and smoke from brush fires

426   (Australia) are commonly observed in January.

427   A significant narrowing in the Z_{clp} north-south distribution over the Atlantic

428   Ocean is apparent in Spring following the conclusion of the Equatorial Africa biomass

429   burning season. Z_{clp} values higher than those observed in winter are apparent over the

430   Atlantic Ocean owing to the Spring activation of Saharan dust sources. Elevated layers

431   (3km and higher) can be observed over the eastern half of the continental US, generally

432   resulting from the transport of carbonaceous aerosols from boreal wild fires in Canada

433   (northeast) and local sources, as well as contribution from transport from Mexico and

434   Central America (southeast). The observed Z_{clp}'s lower than 3 km over the western half

435   of the US are likely associated with local dust production. As a consequence of the

436   activation of dust sources in Central Asia, elevated layers (3km and higher) are apparent

437   over Afghanistan, Turkmenistan, and Uzbekistan. Long range transport of desert dust

438   from the Saharan sources across the Mediterranean, and from sources in Central Asia

439   trigger the spread of dust aerosol layers about 2.5 km high over western and northern

440   Europe. Eastward transport of desert dust following the Spring activation of the Gobi

441   and Taklamakan deserts, and layers of carbonaceous aerosols from biomass burning in

442   Southeast Asia linger over East Asia in layers 2 to 3 km high .

443   An enhanced Summer Z_{clp}, associated with the northward spread of aerosol

444   layers from boreal fires in Canada and Siberia, is observed at about 3 km. The Summer

445   Saharan aerosol layer over the Atlantic Ocean between 10°N and 30°N varies in altitude

446   between 3.5-40 km at the West Coast of Northern Africa going down towards the West,

447   reaching 1.5 km over the Gulf of Mexico. Smoke from biomass burning activity in

448   Central Africa spills over the Southern Atlantic Ocean in an aerosol layer at 2-2.5 km.

449   The Autumn global aerosol height distribution is characterized by an overall Z_{clp}

450   decrease. Except for a height increase over the biomass burning regions in the Southern

451   Hemisphere, Autumn Z_{clp} values are lower than the previous season values by 1 - 2 km

452   over most of the globe. The Saharan Layer Z_{clp} over the Atlantic Ocean reaches values as

453   low as 1.5 km about halfway between Northern Africa and the Gulf of Mexico. The

454   carbonaceous aerosol layer, known as the 'river of smoke', flowing off Southeast Africa

455   along the Indian Ocean at a 1~2 km height Z_{clp} is clearly observed .

456

5. Evaluation of improvements in OMAERUV retrievals

458   A brief discussion of the effect of the algorithm upgrades on retrieved products

459   is presented here. Comprehensive assessments of the OMAERUV products using

460   ground based and other satellite observations are discussed in detail by *Ahn et al.* [2013]

461   and *Jethva et al.* [2013].

462   The effect of using the CALIOP Zclp climatology as input in the OMI inversion

463   algorithm, was evaluated by comparing the optical depth from the OMAERUV algorithm

464   to AERONET observations using both the standard algorithm aerosol height assumption

465   and the aerosol altitude extracted from the CALIOP climatology described here. The

466   assessment exercise was carried out using AERONET measurements at the five sites

467   listed in Table 1, where the presence of elevated dust and smoke layers is routinely

468   observed. Columns 4 through 8 in Table 1 show respectively the resulting correlation

469   coefficient (r), intercept, the rms, and the number of retrievals within 10% (Q_{10}) and 30%

470   (Q_{30}) of the AERONET values, for both the standard aerosol layer height assumption,

471   and the CALIOP provided height information. The standard OMAERUV method of

472   prescribing aerosol layer height of desert dust layers based on a model-generated

473   climatology works fairly well as indicated the correlation coefficients between 0.71 and

474   0.83 at the five locations. Small but important improvement in these statistics is obtained

475   when the CALIOP-based climatology of aerosol layer height. The CALIOP-based

476   approach yields higher correlation coefficients (between 0.74 and 0.84) and slightly

477   smaller intercepts. The improvement is noticeable in terms of the Q_{10} and Q_{30} parameters,

478   defined as the number of points (in percent) within 10% and 30% of the ground truth

479   observations. Q_{10} went up between 3 and 17% at the five sites whereas Q_{30} increased

480   between   3% and 11%. In most cases the effect of using the CALIOP-based aerosol layer

481   height was to reduce AERONET-OMI differences in the winter season when the aerosol

482   layer height is under-estimated by the standard assumption. The observed improvement is

483   smallest in the middle of the Saharan Desert (Tamanrasset site) and increases rapidly

484   away from the dust aerosol source areas with the largest improvement registered at

485   Dakar. The scatter plot in Figure 7 illustrates the resulting OMAERUV AOD

486   improvement in relation to AERONET observations at the Banizoumbou AERONET

487   site.

488   As illustrated in Figure 3, the use of CO measurements as an aerosol tracer has

489   facilitated the identification of carbonaceous aerosols over arid regions, where the

490   distinction between dust and smoke particles would not have been possible without the

491   availability of CO observations. The AIRS CO data has also enabled the detectability

492   and characterization of high levels of boundary layer pollution aerosols undetectable by

493   the previous OMAERUV algorithm without the help of AIRS CO data. Figure 8 depicts

494   the retrieved fields of aerosol optical and single scattering albedo on August 20, 2007

495   over Northeastern China by the previous (top) and current (bottom) versions of the

496   algorithm.

497   **6. Summary and Conclusions**

498   We have documented the use of CALIOP aerosol vertical distribution

499   information and AIRS CO column amounts to provide information on aerosol layer

500   height and aerosol type necessary for the retrieval of AOD and SSA by the OMAERUV

501   algorithm. The combined use in real time of observations from sensors on two different

502   satellites is only possible thanks to the near-simultaneity of A-train observations.

503

504   It has been shown that the combined use of AIRS CO observations and the OMI

505   UV aerosol index provides a way of reliably identifying the absorbing aerosol type when

506   absorbing aerosols have been positively detected via the AI. Because CO is an excellent

507   tracer of carbonaceous aerosols, elevated values of both AI and CO correspond in most

508   cases to the presence of smoke layers whereas the occurrence of high AI values and low

509   CO amounts is associated with layers of desert dust aerosols. Another useful application

510   of the AIRS CO data is the identification of high boundary layer aerosol loads that would

511   otherwise be dismissed as cloud contamination by OMAERUV. Because of the large

512   aerosol load associated with these events over biomass burning regions and Eastern

513   China, it is possible to retrieve both aerosol optical depth and single scattering albedo.

514

515   We made use of time and space collocated CALIOP and OMI observations for

516   the determination of the height of elevated layers of carbonaceous and desert dust

517   aerosols detected by OMI's near UV observations. An effective aerosol layer height was

518   calculated as the attenuated-backscatter-weighted average height obtained from

519   CALIOP's 1064 nm measurements. Observations at 1064 nm were chosen over the 532

520   nm measurements because of apparent saturation effects at the shorter wavelength. The

521   OMI-CALIOP combined analysis was carried out over a 30-month record from July-

522   2006 to December 2008, when instrumental issues affecting the OMI sensor resulted in

523   the loss of the collocation capability.

524   A 30 month climatology of aerosol layer height was calculated. The impact of

525   using CALIOP-based climatology of aerosol layer height was evaluated by comparing

526   OMI retrieved AOD's to AERONET observations at a number of locations in Northern

527   Africa. Validation results indicate that although previous algorithm assumptions on

528   aerosol layer height worked reasonably well, the use of the CALIOP-based climatology

529   produces a noticeable improvement of retrieval results. The CALIOP-based absorbing

530   aerosol layer height climatology and the real-time use of AIRS CO observations have

531   been integrated into the current version of the OMAERUV algorithm.

532

References

Ahn, C., O. Torres, and H. Jethva (2013), Assessment of OMI near UV Aerosol Products. Part 1: Evaluation of Aerosol Optical Depth (*submitted*)

Ahn C., O. Torres, and P.K. Bhartia (2008), Comparison of OMI UV Aerosol Products with Aqua-MODIS and MISR observations in 2006, *J. Geophys. Res*, 113, D16S27, doi:10.1029/2007JD008832

Anderson, T.L., R.J. Charlson, N. Bellouin, O. Boucher, M. Chin, S.A. Christopher, J. Haywood, Y. J. Kaufman, S Kinne, J. A. Ogren, L.A. Remer, T. Takemura, D. Tanre, O. Torres, C.R. Trepte, B.A. Wielicki, D.M. Winker, and H. Yu, Am "A-Train" Strategy for Quantifying Direct Climate Forcing by Anthropogenic Aerosols, Bull. Amer. Met. Soc., December, 2005

Angstrom, A. (1929), On the atmospheric transmission of Sun radiation and on dust in the air, Geogr. Ann., 12, 130-159.

Aumann, H. H., et al. (2003), AIRS/AMSU/HSB on the Aqua mission: Design, science objectives, data products, and processing systems, IEEE Trans. Geosci. Remote Sens., 41, 253–264.

Chahine, M. T. (1974), Remote sounding of cloudy atmospheres, I, The single cloud layer, J. Atmos. Sci., 31, 233– 243.

Chen, Z., O. Torres, M.P. McCormick, W. Smith, and C. Ahn (2012), Comparative Study of aerosol and cloud detected by CALIPSO and OMI, Atmos. Environ., 51, 187-195.

De Graaf, M., P. Stammes, O. Torres, and R.B.A. Koelemeijer (2005a), Absorbing Aerosol Index: Sensitivity Analysis, Application to GOME and Comparison with TOMS, *J. Geophys. Res.,* 110, D01201, doi:10.1029/2004JD005178

De Graaf, M. and Stammes, P.:, (2005b) ,SCIAMACHY Absorbing Aerosol Index – Calibration issues and global results from 2002–2004, Atmos. Chem. Phys., 5, 2385–2394

de Vries Penning, M. J. M., Beirle, S., and Wagner, T. (2009), UV Aerosol Indices from SCIAMACHY: introducing the SCattering Index (SCI), Atmos. Chem. Phys., 9, 9555-9567, doi:10.5194/acp-9-9555-2009.

Dirksen, R. J., K. Folkert Boersma, J. de Laat, P. Stammes, G. R. van der Werf, M. Val Martin, and H. M. Kelder (2009), An aerosol boomerang: Rapid around-the-world transport of smoke from the December 2006 Australian forest fires observed from space, J. Geophys. Res., 114, D21201, doi:10.1029/2009JD012360.

Dubovik, O., B. Holben, T.F. Eck, A. Smirnov, Y.J. Kaufman, M.D. King, D. Tanre, and I. Slutsker (2002), Variability of absorption and optical properties of key aerosol types observed in worldwide locations, *J. Atm. Sci.,* 59, 590-608.

Eck, T.F., B.N. Holben, J.S. Reid, O. Dubovik, A. Smirnov, N.T O'Neill, I. Slutsker, and S. Kinne (1999), Wavelength dependence of the optical depth of biomass burning, urban and desert dust aerosols, *J. Geophys. Res.*, 104, D24, 31333–31349.

Ginoux, P., M. Chin, I. Tegen, J. M. Prospero, B. Holben, O. Dubovik, and S.-J. Lin (2001), Sources and distributions of dust aerosols simulated with the GOCART model, J. Geophys. Res., 106(D17), 20255–20273, doi:10.1029/2000JD000053.

576   Gleason, J., N.C. Hsu and O. Torres, (1998), Biomass burning smoke measured using
577   backscattered ultraviolet radiation: SCAR-B and Brazilian smoke inter annual
578   variability, *J. Geophys Res.,* 103, 31969-31978
579   Gonzalez R., and R. Woods (1992), *Digital Image Processing*, Addison-Wesley
580   Publishing Company, , p 191.
581   Herman, J.R., P.K. Bhartia, O. Torres, C. Hsu , C. Seftor, and E. Celarier (1997), Global
582   Distribution of UV-absorbing Aerosols From Nimbus-7/TOMS data*, J. Geophys. Res.*,
583   102, 16911-16922
584   Hsu, N.C., J.R. Herman, P.K. Bhartia, C.J. Seftor A.M. Thompson, J.F. Gleason, T.F.
585   Eck, and B. N. Holben (1996), Detection of biomass burning smoke from TOMS
586   measurements, *Geophys. Res. Lett.*, 23, 745-748.
587   Jethva, H., O. Torres and C. Ahn (2013), Assessment of OMI near UV Aerosol Products.
588   Part 2: Comparison of Single Scattering Albedo to Ground-Based AERONET
589   Observations in Biomass Burning and Dust Environments (*submitted*)
590   Jethva, H. and O. Torres (2011), Satellite-based evidence of wavelength-dependent
591   aerosol absorption in biomass burning smoke inferred from Ozone Monitoring
592   Instrument, Atmos. Chem. Phys., 11, 10541-10551, doi:10.5194/acp-11-10541-201.
593   Levelt, P. F., E. Hilsenrath, G. W. Leppelmeier, G. H. J. van den Ooord, P. K. Bhartia, J.
594   Taminnen, J. F. de Haan, and J. P. Veefkind (2006), Science objectives of the Ozone
595   Monitoring Instrument, IEEE Trans. Geosci. Remote Sens., 44(5), 1093–1101.
596   Levy, R. C., Remer, L. A., Kleidman, R. G., Mattoo, S., Ichoku, C., Kahn, R., and
597   Eck, T. F., (2010), Global evaluation of the Collection 5 MODIS dark-target aerosol
598   products over land, Atmos. Chem. Phys., 10, 10399-10420, doi:10.5194/acp-10-
599   10399-2010.
600   Luo, M., C. Boxe, J. Jiang, R. Nassar, and N. Livesey, (2010), Interpretation of Aura
601   satellite observations of CO and aerosol index related to the December 2006 Australia
602   fires, Remote Sensing of Environment, 114, 2853-2862.
603   McMillan, W. W., C. Barnet, L. Strow, M. T. Chahine, M. L. McCourt, J. X. Warner, P.
604   C. Novelli, S. Korontzi, E. S. Maddy, and S. Datta (2005), Daily global maps of
605   carbon monoxide from NASA's Atmospheric Infrared Sounder, *Geophys. Res. Lett.,*
606   32, L11801, doi:10.1029/2004GL021821.
607   Pan, L., J.C. Guille, D. P. Edwards, and P.L. Bailey (1998), Retrieval of tropospheric
608   carbon monoxide for the MOPITT experiment, *J. Geophys. Res.*, 103, 32277-32290.
609   Savtchenko A., R. Kummerer, P. Smith, A. Gopalan, S. Kempler, and G. (2008),
610   Leptoukh, A-Train Data Depot: Bringing Atmospheric Measurements Together, IEEE
611   Trans. Geos. Rem. Sens., 46, No. 10, 2788-2795
612   Seftor, C.J., N.C. Hsu, J.R. Herman, P.K. Bhartia, O. Torres, W.I. Rose, D.J. Schneider,
613   and N. Krotkov (1997), Detection of volcanic ash clouds from Nimbus7/total ozone
614   mapping spectrometer, *J. Geophys. Res.*, 102, 16,749-16,759
615   Sinha, P., P. V. Hobbs, R. J. Yokelson, I. T. Bertschi, D. R. Blake, I. J. Simpson, S. Gao,
616   T. W. Kirchstetter, and T. Novakov (2003), Emissions of trace gases and particles
617   from savanna fires in southern Africa, *J. Geophys. Res.*, 108, 8487,
618   doi:10.1029/2002JD002325.
619   Susskind, J., C. D. Barnet, and J. M. Blaisdell (2003), Retrieval of atmospheric and
620   surface parameters from AIRS/AMSU/HSB data in the presence of clouds, IEEE
621   Trans. Geosci. Remote Sens., 41, 390– 409.

622 Swap, R.J., H.J. Annegarn, J.T. Suttles, M.D. King, S. Platnick, J.L. Privette, and R.J.
623   Scholes (2003), Africa Burning: A thematic analysis of the Southern African Regional
624   Science Initiative (SAFARI 2000), *J. Geophys. Res.,* 108(D13), 8465,
625   doi:10.1029/2003JD003747
626 Toledano, C., M. Wiegner, S. GROß, V. freudenthaler, J. Gasteiger, D. Muller, A.
627   Schladitz, B. Weinzierl, B. Torres, and N.T. O'Neill (2011), Optical properties of
628   aerosol mixtures from sun-sky radiometry during SAMUM-2, *Tellus* 63B, 635-648.
629 Torres O., P.K. Bhartia, J.R. Herman and Z. Ahmad (1998), Derivation of aerosol
630   properties from satellite measurements of backscattered ultraviolet radiation.
631   Theoretical Basis, *J. Geophys. Res.*, 103, 17099-17110
632 Torres, O., P.K. Bhartia, J.R. Herman, A. Syniuk, P. Ginoux, and B. Holben (2002), A
633   long term record of aerosol optical depth from TOMS observations and comparison to
634   AERONET measurements, *J. Atm. Sci.,* 59, 398-413
635 Torres, O., A. Tanskanen, B. Veihelman, C. Ahn, R. Braak, P. K. Bhartia, P. Veefkind,
636   and P. Levelt (2007), Aerosols and surface UV products from OMI Observations: an
637   overview, *J. Geophys. Res.,* 112, D24S47, doi:10.1029/2007JD008809
638 Turquety, S., Hurtmans, D., Hadji-Lazaro, J., Coheur, P.-F., Clerbaux, C., Josset, D., and
639   Tsamalis, C. (2009), Tracking the emission and transport of pollution from wildfires
640   using the IASI CO retrievals: analysis of the summer 2007 Greek fires, Atmos. Chem.
641   Phys., 9, 4897-4913, doi:10.5194/acp-9-4897-2009.
642 Winker, D. M., J. Pelon, and M. P. McCormick, 2003: "The CALIPSO mission:
643   Spaceborne lidar for observation of aerosols and clouds", *Proc. SPIE*, 4893, pp. 1-11.
644
645
646
647
648
649
650
651
652
653
654
655
656
657
658
659
660
661
662
663
664
665
666
667

668 **Figure Captions**

669

670   **Figure 1.** Graphic description of OMAERUV inversion scheme.

671   **Figure 2.** OMAERUV Aerosol Index on July 7, 2006 (a), AIRS CO amounts (b)

672   **(c)** Aerosol type classification

673   **Figure 3.** Aerosol type over Africa on August 27, 2007 (see text for details)

674   **Figure 4.** CALIOP-measured attenuated backscatter profiles at 532 nm (solid line) at

675   1064 nm (dotted line) over Amazonia (left) and Saharan Desert (right).

676   **Figure 5.** Sample derived aerosol layer height and CALIOP-measured 1064 nm

677   backscatter for three aerosol episodes: top: top; middle, middle; bottom: bottom.

678   **Figure 6.** Monthly average aerosol layer height.

679   **Figure 7.** Evaluation of AOD retrieval using standard aerosol layer height assumption

680   (left) and CALIOP climatology (right) at the Banizoumbou site.

681   **Figure 8**. Retrieved AOD and SSA at 388 nm from the previous (a, b) and improved (c,

682   d) OMI UV algorithm over Northeastern China on Aug 20, 2007.

683

684

685

686

687

688

689

690

691

692

693

694

695

696

697

698

699

700   Table 1

AERONET Site	Location Lat. Lon.	Number points	R Std Cal	Intercept Std. Cal	RMS Std. Cal	Q_{10} Std Cal	Q_{30} Std Cal
Agoufou	15.3N 1.5E	184	0.82 0.83	0.13 0.10	0.17 0.16	50 58	64 71
Tamanrasset	22.8N 5.5E	98	0.83 0.84	0.09 0.08	0.10 0.10	60 63	66 69
Banizombou	13.5N 2.7E	182	0.71 0.75	0.21 0.17	0.19 0.16	45 53	57 67
Dakar	14.4N 17.0W	163	0.73 0.74	0.14 0.12	0.19 0.15	39 56	58 69
IER_Cinzana	13.3N 5.9W	118	0.79 0.83	0.09 0.08	0.21 0.17	35 47	50 60

701

702

703

704

705

706

707

708

709

710

711

712

713

714

715

716

717

718

719

720

721

722

723

724

725

726

Aerosol Type Determination

AI ≥ 0.8 & COI > 2.2 N.H (1.8 S.H)
OR
COI > 2.8 N.H (2.5 S.H)? → Yes → CB

No

AI ≥ 0.8
OR
Arid surface type? → Yes → DD

No

SF

Algorithm Flagging Scheme

ΔR ≤ 0.07
OR
CB & ΔR ≤ 0.08 & AI ≥ 0.3
OR
CB & R388 < 0.16
OR
CB & AI < 0.5? → Yes → Flag 0

No

R388 < 0.30 & AI ≥ 0.8? → Yes → Flag 1

No

No Retrieval

Best Guess ALH Determination

SF? → Yes → ALH = 0.0 km

No

CB & AI < 0.5? → Yes → ALH = 1.5 km

No

Is CALIOP ALH climatology available? → Yes → Extract ALH for both CB & DD

No

For DD, ALH given by CTM-generated climatology
For CB within ± 30°, ALH = 3km
For CB beyond ± 45°, ALH = 6km
ALH interpolated between 3 and 6 km for 30° to 45°

Retrieval Method at std ALH's
(0, 1.5, 3, 6 and 10 km)

-Two-channel /two-parameter (τ, ω_0)

-One-channel/one-parameter (τ)

CB → Two channel retrieval
DD & AI ≥ 0.8 → Two channel retrieval
DD & AI < 0.8 → Single channel retrieval
SF & AI ≥ 0.5 → Two channel retrieval
SF & AI < 0.5 → Single channel retrieval

727

728   Figure 1

729

730

731

732

733

734

735

736

737

738

739

740

741

742

743

744

745

746

747

748
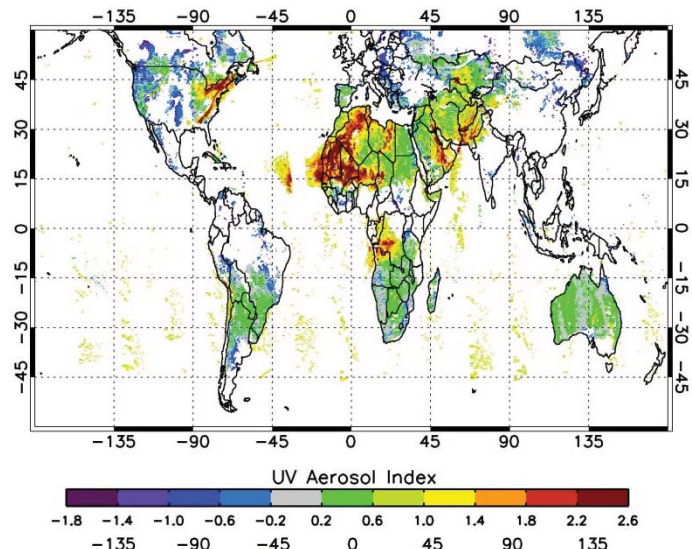
749
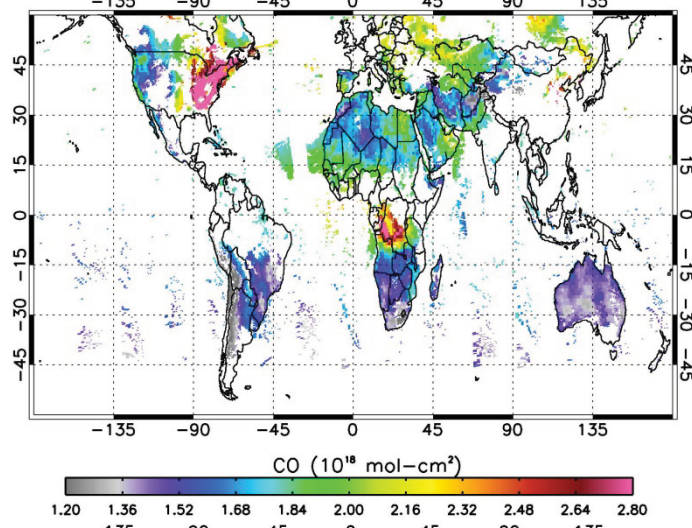
750
751
752   Figure 2

30
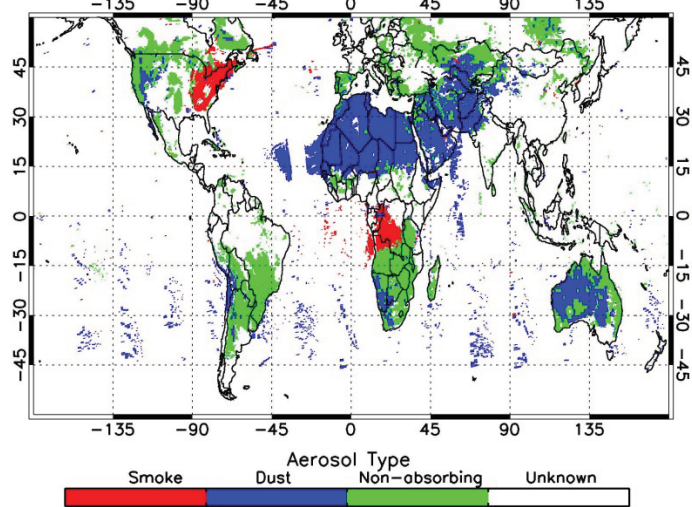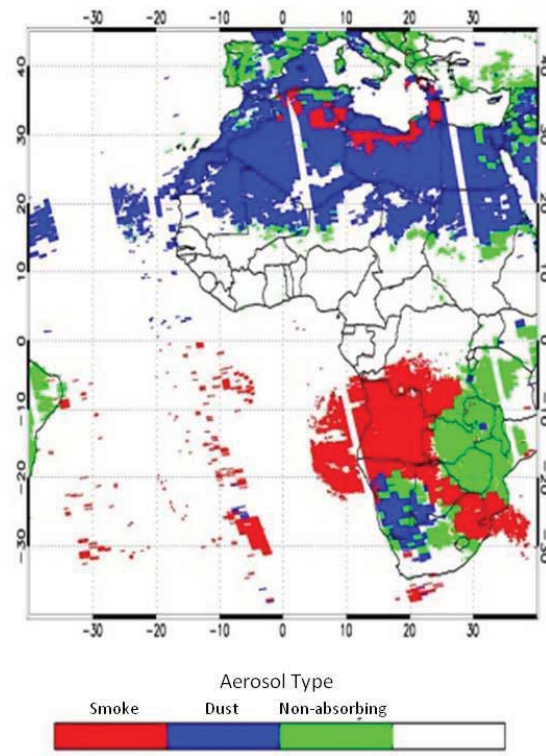
Figure 3

753
754
755
756
757
758
759
760
761
762
763
764
765
766
767
768
769
770
771
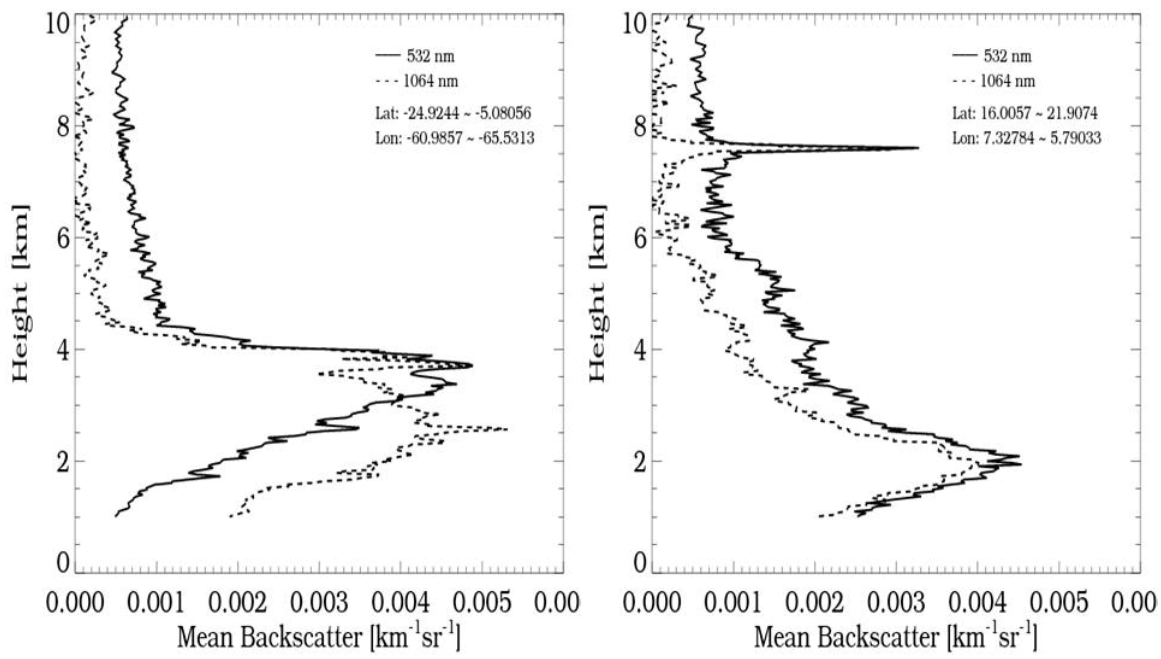
Figure 4.

791
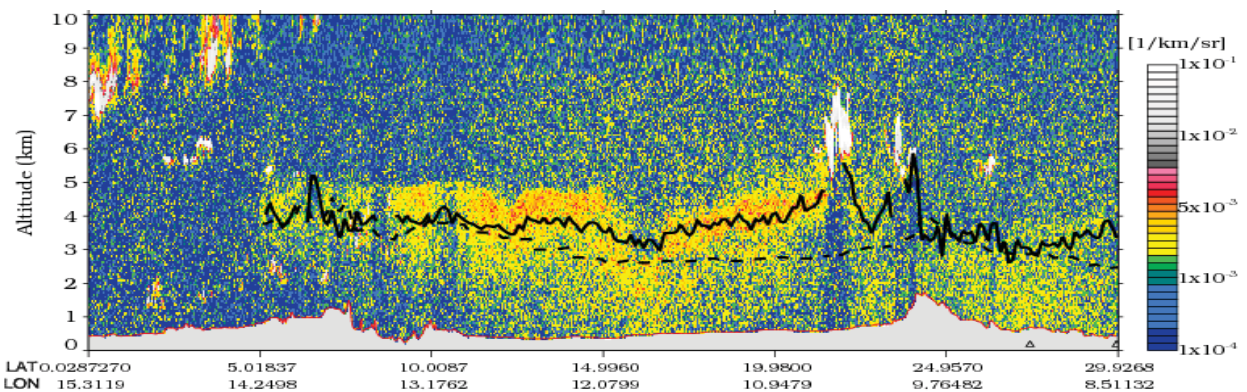
792
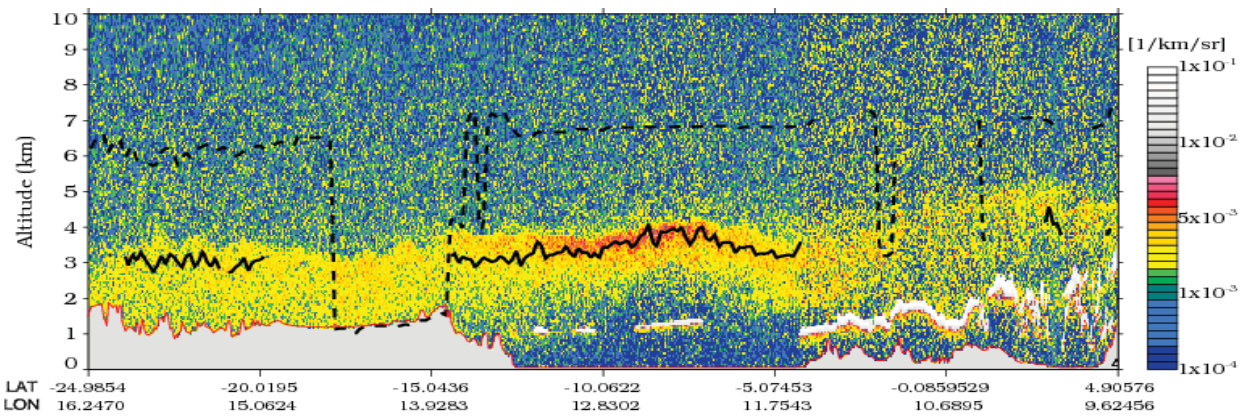
793
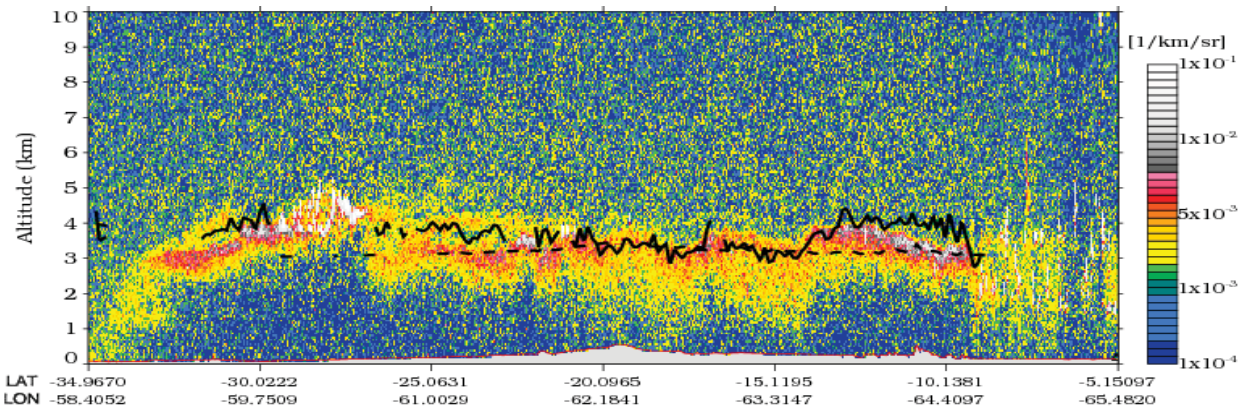
794

795   Figure 5.

796

797

798

799

800

801

802
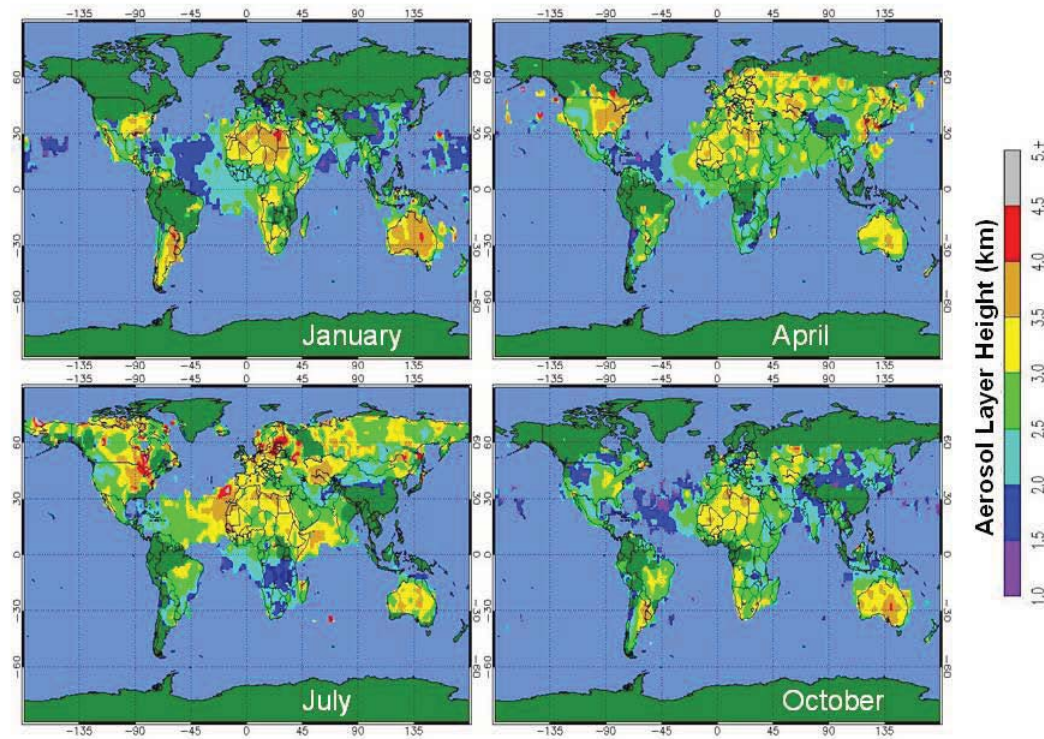
803

804   Figure 6

805

806

807

808

809

810

811

812

813

814

815

816

817

818

819
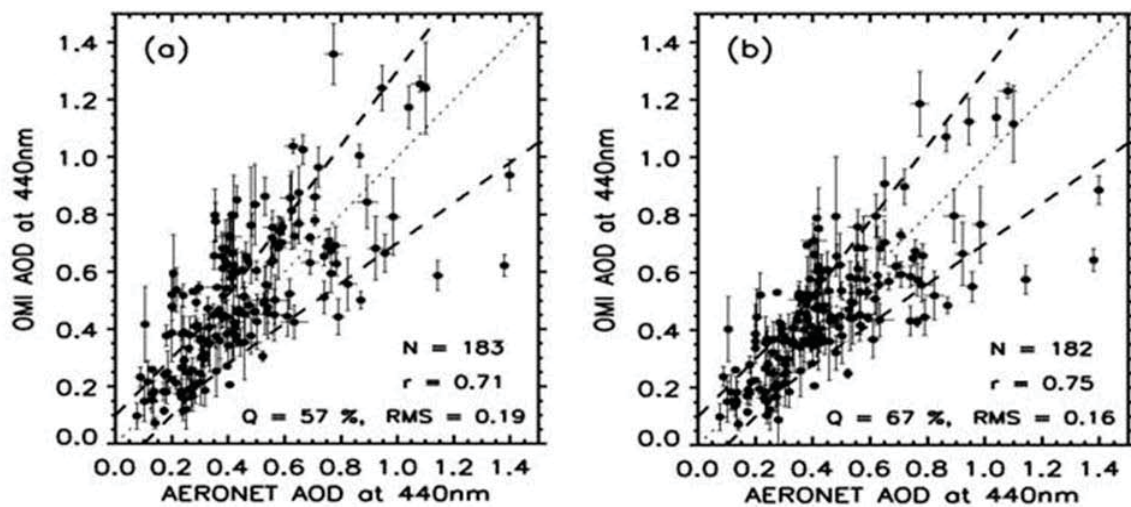
820

821   Figure 7

822

823

824

825

826

827

828

829

830

831

832

833

834

835

836

837

838

839

840

841

842

843
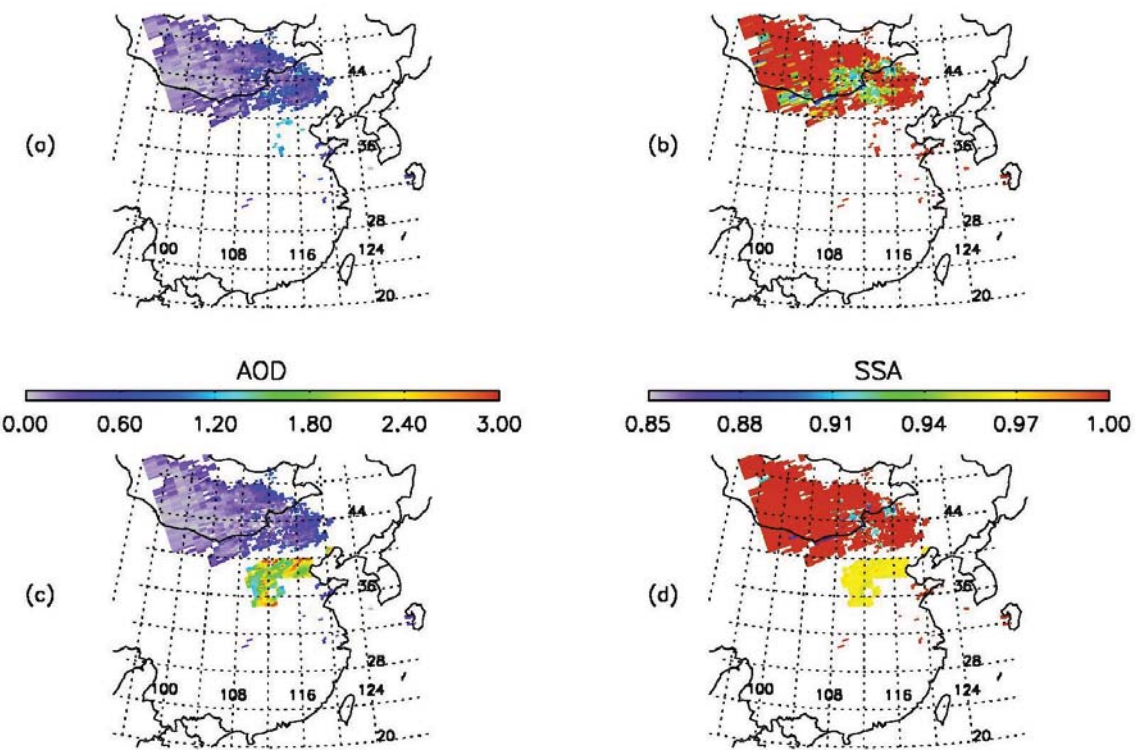
844
845   Figure 8.

846

847

848

849

850

851

852

853

854

855

856

857

858

859

860